NUMERICAL INVESTIGATION OF THE FLOW OVER A GOLF BALL IN THE SUBCRITICAL AND SUPERCRITICAL REGIMES

Clinton Smith[1], Nikolaos Beratlis[2], Elias Balaras[2], Kyle Squires[1], and Masaya Tsunoda[3]

ABSTRACT

Direct numerical simulation (DNS) is applied within the framework of an immersed boundary approach to understand the role of surface dimpling on the flow over a golf ball. In the present study, DNS results are reported for simulations in the subcritical (Re = 2.5×10^4) and supercritical regimes (Re = 1.1×10^5) using as many as 1.2×10^9 grid points. Flow visualizations reveal the differences in separation characteristics between the two Reynolds numbers. Profiles of the mean velocity indicate that the flow detaches completely at approximately 90 degrees in the subcritical case (measured from the stagnation point at the front of the ball), while in the supercritical regime there are alternating regions of reattachment and separation within dimples with complete detachment around 110 degrees. Energy spectra highlight frequencies associated with vortex formation over the dimples prior to complete detachment in the supercritical regime. Reynolds stresses quantify momentum transport in the near-wall region, showing that the radial and axial stresses increase around 90 degrees for the subcritical case. In the supercritical regime these stress components alternately increase and decrease, corresponding to local separation and reattachment. Prediction of the drag coefficient for both Reynolds numbers is in reasonable agreement with measurements.

INTRODUCTION

Since the accidental discovery of drag reduction by surface roughening, golfers and equipment manufacturers have sought to optimise dimple patterns to reduce drag (e.g., see Smits and Ogg 2003). Optimisation of dimple patterns – their density, shape, and size – requires an understanding of the mechanisms that lead to drag reduction by surface dimpling.

Relevant to the current contribution are studies of the flow over smooth spheres. Previous work, both experimental and computational has been instrumental in understanding the role of boundary layer characteristics on separation (e.g., see Maxworthy 1969, Achenbach 1972). As is also true for the circular cylinder, the sphere is known for its drag crisis, a reflection of the substantial differences in separation characteristics of laminar and turbulent boundary layers.

A dramatic effect of dimples is to induce the drag crisis at substantially lower Reynolds numbers than occurs for a smooth sphere. The effect of surface dimpling has been investigated by Davies (1949) who measured the aerodynamic forces on a spinning golf ball at Re = 9.4×10^4 in experiments that measured the impact point after the ball was dropped through the horizontal flow in a wind tunnel. Bearman and Harvey (1976) made the next major contribution by measuring the aerodynamic forces acting on a spinning golf ball over a range of Reynolds numbers, assessing the effect of spherical and hexagonal dimples. Smits and Smith (1994) measured the flight characteristics

of a spinning golf ball in an indoor range and developed an aerodynamic model for golf ball flight. Most recently, Choi, Jeon and Choi (2006) measured the drag on a non-rotating golf ball and gathered turbulence statistics of the flow in order to understand how dimples promote turbulence and lead to drag reduction. Choi et al (2006) proposed that the drag reduction mechanism is related to the development of a shear layer instability that leads to higher momentum near the wall, causing local flow reattachment and a delay in complete separation, and in turn a significant reduction in drag.

Assessing the separation characteristics of flow around a golf ball and investigating the influence of dimples on drag reduction are excellent candidates for study using direct numerical simulation (DNS), the most fundamental simulation strategy for computation of turbulent flows. DNS is especially appropriate for flows that inter-mingle the effects of separation and transition since these features strongly challenge other simulation strategies that require empirical input via the introduction of turbulence models.

The over-arching objective of this work is the application of DNS to prediction of the flow over a golf ball in order to gain insights into the role of surface dimpling on flow physics. In the present study DNS results are reported for simulations performed pre- and post-drag crisis; in particular, for computations around a non-rotating ball in the subcritical (Re = 2.5×10^4) and supercritical regimes (Re = 1.1×10^5).

The numerical approach is based a non-boundary-conforming methodology. Such methods relax the requirement that the grid conforms to the boundary, and instead represent a complex body using an appropriate treatment of solution variables at grid points near the body. The advantages of these techniques are that grid generation is simplified, especially in the case of a moving body and, that efficient flow solvers can be employed. Immersed boundary methods represent a subset of these techniques, and are adopted in this work, in which forces are used to represent the effect of an object in the flow (e.g., see Yang and Balaras 2006).

COMPUTATIONAL APPROACH
Geometry and Grid

A geometry supplied by Srixon and comprised of approximately 300 spherical dimples is used in this study. The surface of the ball is discretized with a mesh of surface triangles connected by nodes. The dimple geometry on the golf ball has an axis of one-fifth symmetry. The symmetry axis is aligned with the freestream direction (c.f. Figure 1a). The existence of the symmetry axis and its

[1] Mechanical and Aerospace Engineering Department, Arizona State University, Tempe, AZ 85287 USA
[2] Fischell Department of Bioengineering, University of Maryland, College Park, MD 20742 USA
[3] Sumitomo Rubber Industries Ltd., Kobe, Japan

alignment with the freestream coordinate is advantageous since statistical sample can be improved by averaging over azimuthal planes, as well as time. For the statistics presented below, samples were collected in the five azimuthal planes shown in Figure 1a.
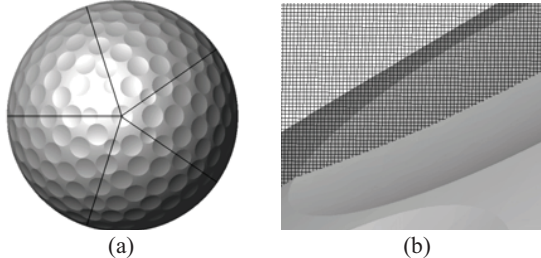

(a)   (b)

Figure 1 – Golf ball dimple geometry: (a) one-fifth symmetry axis alignment; (b) grid resolution from the Re = 1.1×10^5 simulation, 100 points in streamwise (horizontal) direction

Simulations are conducted for a subcritical case at a Reynolds number of 2.5×10^4 and a supercritical case at a Reynolds number of 1.1×10^5. The grid sizes in the radial, azimuthal, and axial directions are summarized in Table 1.

Table 1: Grid resolution

Coordinate	Re = 2.5×10^4	Re = 1.1×10^5
Radial (R)	536	814
Azimuthal (θ)	252	502
Axial (Z)	2502	3002
Total grid points	337×10^6	1.2×10^9

The radial and axial grid point distributions were clustered to refine the grid near the golf ball. This was accomplished by modifying stretching ratios, e.g., a radial stretching ratio in the Re = 2.5×10^4 case changes from 0.984 ($\Delta R / D \sim 1 \times 10^{-2}$) near the center-line to 0.999 ($\Delta R / D \sim 8 \times 10^{-4}$) near the region of flow detachment. The radial and axial grids were then smoothed in order to avoid abrupt changes in spacing using a stencil that weighted the coordinate value of a particular point twice as much as the point before and after it. As depicted in Figure 1b, the grid near the dimple surface maintains an approximately uniform resolution in order to capture the velocity gradients and small-scale structures that develop over the ball. This approximate uniformity of the grid near the surface is maintained for both Reynolds numbers. For either Reynolds number, the azimuthal grid spacing is constant, finer by a factor of two at the higher Reynolds number. For the low Reynolds number flow there are approximately 120 points across the dimple at the top/bottom of the ball (90 degrees from the stagnation point) while for the high Reynolds number case the mesh resolution at the top/bottom of the ball is approximately 160 points across the dimple.

Numerical Method and Simulation Overview

The governing equations are solved on a staggered grid in cylindrical coordinates and are integrated in time using a fractional step formulation, in which an implicit (Crank-Nicholson) method is applied to the viscous terms in the azimuthal direction. All other terms are advanced with an explicit third-order Runge-Kutta scheme. Spatial derivatives are approximated using second-order central differences. The large, sparse, banded matrix associated with the solution of the Poisson equation is inverted using a direct method (Balaras and Yang 2005).

An immersed boundary methodology is applied in which the golf ball surface is immersed in the background fluid grid and does not align with this grid. The solution in the vicinity of the golf ball is reconstructed to enforce the prescribed boundary conditions on the surface. This is accomplished using a direct forcing approach as described in Yang and Balaras (2006) and is comprised of three steps: (a) tag all the points as fluid points, body points, or forcing points (c.f. Figure 2), (b) search for the intersections of the forcing points with the immersed boundary, and (c) calculate a reconstruction matrix needed to enforce the appropriate velocity boundary conditions for each forcing point.

Solutions are obtained in a domain that extends 10D (where D is the golf ball diameter) in the radial direction and 40D in the axial direction. The center of the golf ball is 10D from the inlet to the computational domain (corresponding to the front stagnation point at 9.5 diameters from the inlet).

The flow solver is parallelized using domain decomposition and message-passing interface. The code exhibits linear scaling for computations performed using as many as 500 processors on a range of meshes up to 1.2×10^9 points. Integration of the flow over 96 hours yields 2.5 time units for the subcritical regime, and 0.25 time units for the supercritical regime (the time axis is non-dimensionlized using D / U, where U is freestream velocity).
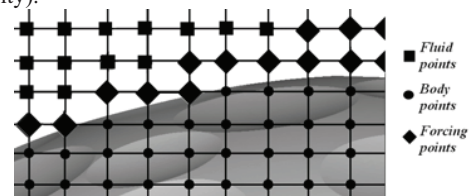

Figure 2 – Immersed golf ball with fluid points, body points, and forcing points

RESULTS
Visualization: Vorticity, Velocity, and Pressure

Visualizations of the instantaneous azimuthal vorticity near the golf ball in Figure 3 provide one illustration of the effect of the Reynolds number on flow separation characteristics. In the subcritical case (Figure 3a), separation does not appear strongly influenced by the dimples, and roll-up of the shear-layer occurs following boundary layer detachment. In the supercritical case (Figure 3b), visualization of the instantaneous vorticity reveals intriguing structures that have length scales comparable to the dimple dimensions. Figure 3b shows that within dimples there are shear layers that develop following detachment of the flow from the leading edge of the dimple, a similar feature being advanced by Choi et al (2006) based on their measurements
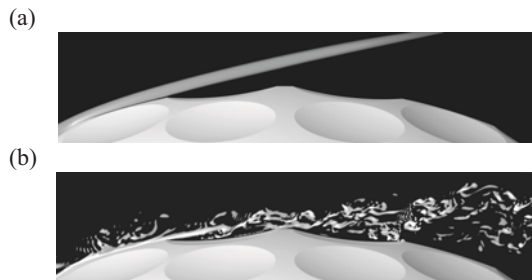
(a)

(b)

Figure 3 – Contours of azimuthal vorticity; (a) Re = 2.5×10^4; (b) Re = 1.1×10^5

Further magnification of the near-wall flow for both regimes is depicted in Figure 4. Contours of the azimuthal vorticity are plotted on an axial plane along with contours of the streamwise velocity in azimuthal planes. For the subcritical case (Figure 4a), the azimuthal vorticity exhibits relatively little variation as the flow evolves across a dimple near the location of flow detachment. As the flow evolves from the front to the rear of the same dimple in the supercritical case (Figure 4b), local detachment leads to small-scale structures resulting from the shear-layer development over the dimple. These small-scale structures (produced by the shear layer over the center of the dimple in Figure 4b) are being advected downstream by the bulk flow.
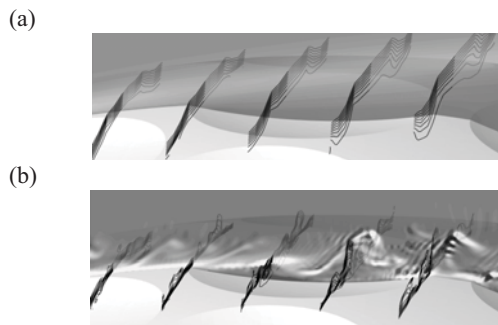
(a)

(b)

Figure 4 – Contours of azimuthal vorticity in an axial plane (background) and streamwise velocity in azimuthal planes in dimples near flow detachment; (a) Re = 2.5×10^4; (b) Re = 1.1×10^5

The structures highlighted in Figure 3b and Figure 4 for the high Reynolds number increase the momentum of the near-wall flow and lead to local reattachment as the flow exits the dimple. This process repeats through several dimples until complete detachment occurs, as displayed in Figure 5. Here, time-averaged contours of the streamwise velocity are displayed at increasing angles from the stagnation point in an azimuthal plane.
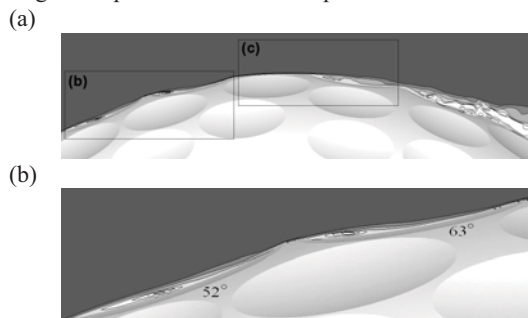
(a)

(b)

(c)

Figure 5 – Time-averaged contours of the streamwise velocity, Re = 1.1×10^5: (a) complete view (b) view at 52°, 63°; (c) view at 74°, 84° (angles measured from stagnation point at the front of the golf ball to the dimple centers)

Figure 5b shows that the flow at 52 degrees and 63 degrees detaches downstream of the leading edge of the dimple. The flow appears to reattach to the surface as it exits the dimple at 63 degrees, as depicted in Figure 5c. Around 74 degrees, the flow remains attached until it traverses the dimple at 84 degrees. Even as the flow exits the dimple at 84 degrees, it appears to reattach to the small portion of the golf ball surface before it detaches again around 96 degrees (not shown)

The flow patterns within dimples and in the region of complete separation are depicted in Figure 6. The subcritical case displays the mean flow which follows the boundary until detachment at around 84 degrees. This separation region is characterized by the recirculation apparent in Figure 6a. The supercritical case shows regions of local recirculation within individual dimples in Figures 5a-c and 6b which transport momentum into the near-wall region and ultimately delay complete detachment until around 110 degrees.
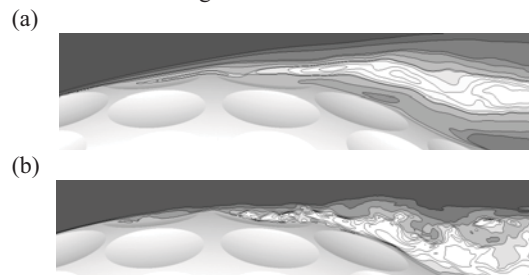
(a)

(b)

Figure 6 – Time-averaged contours of streamwise velocity; (a) Re = 2.5×10^4; (b) Re = 1.1×10^5

Contours of the instantaneous pressure coefficient (C_P) on the surface of the golf ball reveal another view of the effect of the dimples in both physical regimes.
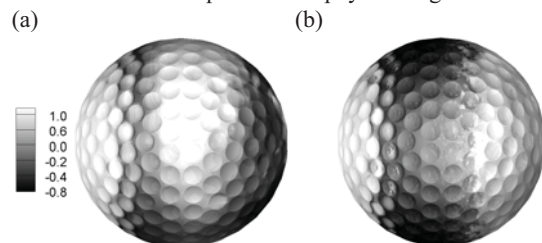
(a)   (b)

Figure 7 – Contours of the pressure coefficient on the surface (side view): (a) Re = 2.5×10^4 (b) Re = 1.1×10^5

The stagnation point and associated region of high pressure is displayed in Figure 7a for the subcritical case, and in Figure 7b for the supercritical Reynolds number. The pressure coefficient decreases as the flow accelerates from the front stagnation point around the ball. For both

Reynolds numbers, C_p decreases to -0.6 around 84 degrees from the stagnation point. In the subcritical regime, the pressure coefficient displays an increasing trend from -0.6 at 84 degrees to approximately -0.3 on the leeward side of the golf ball, corresponding to the behavior of the pressure coefficient for a smooth sphere at a subcritical Reynolds number (e.g., see Achenbach 1972). In the supercritical case, the pressure coefficient decreases from -0.6 at 84 degrees to approximately -0.8 around 90 degrees, eventually recovering to C_p = -0.6 near the line of complete flow detachment around 110 degrees.
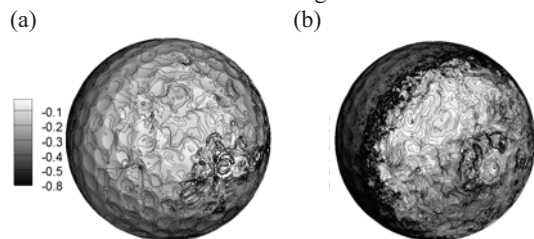
(a)   (b)

Figure 8 – Contours of the pressure coefficient on the surface (leeward side): (a) Re = 2.5×10^4 (b) Re = 1.1×10^5

Contours of the pressure coefficient on the leeward side of the golf ball (Figure 8a,b) display the chaotic effects from the impinging turbulent structures being generated downstream of separation and in the near wake. The effect of the dimples seems to be slight for the subcritical case, as the behavior of the pressure is similar to a smooth sphere in the subcritical regime. For the supercritical Reynolds number, the dimpling appears to have a greater contribution, as it leads to an opposite trend in the pressure (compared to the subcritical case) and corresponds to delayed flow detachment.

Statistical Features

Averaged values of the drag are summarized together with experimental measurements for both Reynolds numbers in Figure 9. The values shown in Figure 9 have been obtained from averages of the force history acquired over approximately 20 D / U time units from the subcritical case, and 15 D / U time units from the supercritical case. For the subcritical regime, 20 time units corresponds to 3-4 vortex-shedding cycles. In the supercritical case, 15 time units corresponds to 8-10 vortex-shedding cycles.
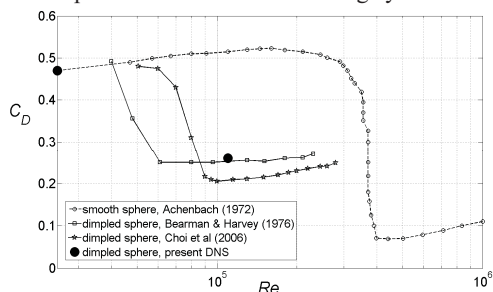

Figure 9 –Drag coefficient from current DNS along with measurements from Achenbach (1972), Bearman and Harvey (1976), and Choi et al (2006)

As shown in Figure 9, the DNS results are in the range of the measurements reported by Achenbach (1972), Bearman and Harvey (1976), and Choi et al (2006). DNS

of the subcritical case at Re = 2.5×10^4 yields C_D = 0.47, close to the value for a smooth sphere of C_D = 0.45 reported by Achenbach (1972) at the same Reynolds number, implying a similar separation process in the flow around a golf ball at this Reynolds number. DNS of the supercritical case at Re = 1.1×10^5 leads to C_D = 0.26 that is nominally higher than the measurements of Bearman and Harvey (1976) (Re = 4.0×10^4 to Re = 2.4×10^5) and approximately two percent higher than the measurements of Choi et al (2006) (Re = 5.0×10^4 to Re = 2.8×10^5). One metric that characterizes the geometries, and differs among the studies, is the dimensionless dimple depth, k / D, where k represents the depth of a dimple and D is the ball diameter. In Bearman and Harvey, k / D = 9.0×10^{-3}, for Choi et al k / D = 4.0×10^{-3}, and the present DNS has k / D_{max} = 6.0×10^{-3}. The dimple geometry, along with related factors such as the overall number and distribution of dimples for the different cases, contribute to the changes in the drag between the experiments and simulations.

Velocity profiles in a cylindrical coordinate system shown in Figure 10 were acquired at several locations in the symmetry planes (c.f. Figure 1). The location of the profiles are shown in Figure 10 and numbered 1 through 7; the profile is acquired at 50 points along each of the surface-normal lines shown. The sampling locations within dimples (locations 1, 2, 4, 6) and on the outer surface of the golf ball (locations 3, 5, 7) were chosen to gather statistics at the locations where the flow is locally detaching and reattaching (c.f. Figure 5).
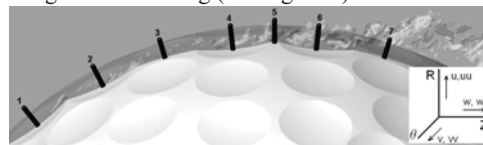

Figure 10 – Profile locations in each of the symmetry planes; background contour shows the azimuthal velocity at Re = 1.1×10^5 (angle measured from stagnation point in a symmetry plane): location 1 - 52°; location 2 - 63°; location 3 - 74°; location 4 - 84°; location 5 - 90°; location 6 - 96°; location 7 - 106°

Statistics of the velocity field acquired at these locations are averaged in time and in space (azimuthally). For each location, the radial and axial velocity components are displayed along the wall-normal direction in Figure 11a-e. The azimuthal component is nearly zero for both Reynolds numbers, and is therefore not shown. Since the profiles are acquired at different points in the domain, the normal coordinate n/D differs slightly (since the sampling points along a normal line originate within a dimple or on the outer surface).
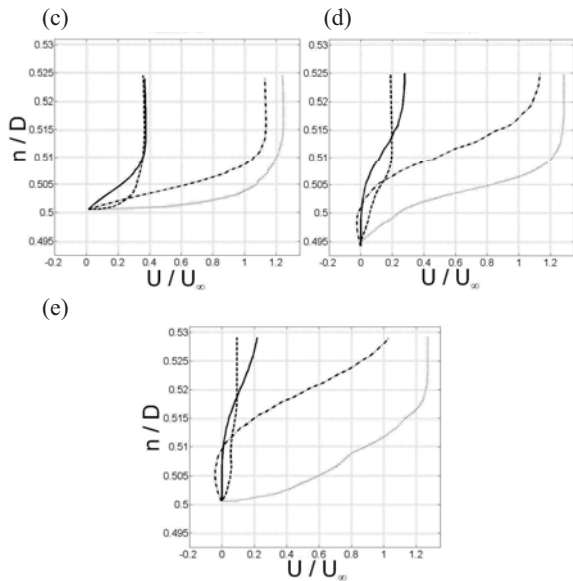
(a)   (b)

(c)   (d)

(e)
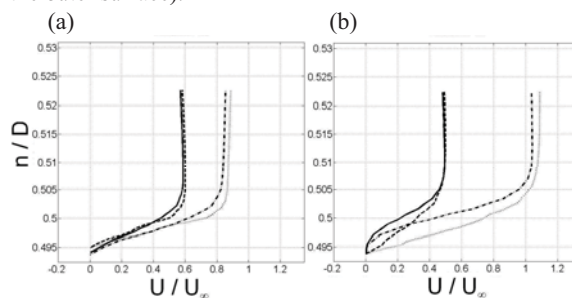
Figure 11 – Mean velocity profiles at locations 1-5 in frames (a)-(e), respectively. —— radial Re = 2.5×10^4; —·— axial Re = 2.5×10^4; – – – radial Re = 1.1×10^5; ···· axial Re = 1.1×10^5

Mean velocity profiles for the subcritical case in Figure 11 quantify the behavior suggested by the visualizations. Locations 1-3 (Figure 11a-c) depict velocity profiles that appear laminar-like. Slight reversal of the flow is observed in the streamwise average at location 4 (Figure 11d), with increasing reversal at location 5 (Figure 11e). Non-zero values of the azimuthal component are also observed at location 5, showing the three-dimensional structure of the flow at and past the point of detachment. For the subcritical case, flow detachment begins as early as location 4 (84 degrees) and appears to be complete around 90 degrees (c.f. Figure 6a).

For the high Reynolds number case, the mean velocity profiles also quantify the behavior illustrated by the flow visualizations. For the supercritical flow, it is locations 1-2 (Figure 11a-b) that have laminar-like velocity profiles. The velocity field at location 4 (Figure 11d) may be affected by the Kelvin-Helmholtz type instabilities in the dimple, as shown by the slight reduction of the streamwise component at approximately n / D = 0.5. Profiles at locations 3 and 5 (Figure 11c,e) suggest high rates of momentum transfer. These mean profiles indicate that the flow detachment begins further into the wake for the supercritical case (approximately 110 degrees, c.f. Figure 6b).

Additional insight into the flow physics is provided by the frequency spectra of the velocity. The flow field was sampled at locations near the ball to extract the high-frequencies of vortex formation in the shear layers. Time series were acquired in the shear layer that develops over the dimple at 96° from the stagnation point (c.f. Figure 10) in the symmetry planes. The resulting spectra of the radial velocity are shown in Figure 12.
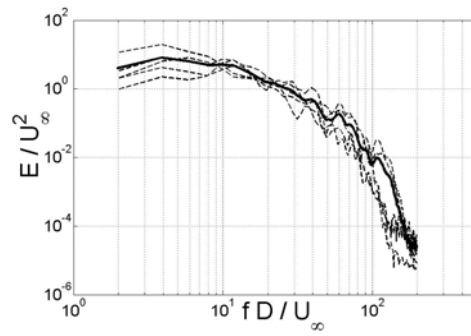

Figure 12 – Energy spectra of radial velocity at 96°, Re = 1.1×10^5: – – – individual plane results,—— spatially-averaged result

The spectra highlight the energy of the flow near complete detachment. The figure indicates secondary peaks at higher Strouhal numbers around 60 and 100, which are comparable to estimates of the frequencies associated with the small structures over the dimples deduced from visualizations.

Momentum transport from the fluctuating velocity field is analyzed via investigation of the Reynolds stresses. Statistics of the flow for the subcritical case have been computed from averages over approximately 2.5 time units and for the supercritical case over approximately 0.5 time units, sufficient to elucidate trends though not statistically converged.

As with the mean velocity, the Reynolds stresses are averaged in the azimuth (again exploiting the symmetry of the geometry). Reynolds stress trends for the low Reynolds number case are shown in Figure 13 and for the supercritical regime in Figures 14 - 16.
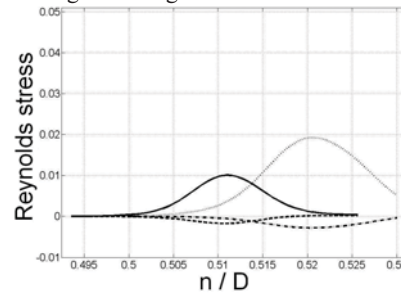

Figure 13 – Reynolds stress, Re = 2.5×10^4: —— ww, location 4; – – – uw, location 4; ···· ww, location 5; —·— uw, location 5

The averaged Reynolds stress for the subcritical case in Figure 13 confirm the physical behavior suggested by the averaged velocity in Figure 11. As the flow evolves from the dimple at 84 degrees to 90 degrees, the fluctuations of *ww* (axial-axial) and *uw* (radial-axial) (c.f. coordinate system in Figure 10) increase by a factor of two. The largest value of the Reynolds stress tensor (over all sampled locations) is observed at n / D = 0.52 in location 5, which is within the detached shear layer. The increased momentum transport from the fluctuating velocity field at locations 4 and 5 is consistent with the apparent flow reversal depicted in Figure 11d,e.
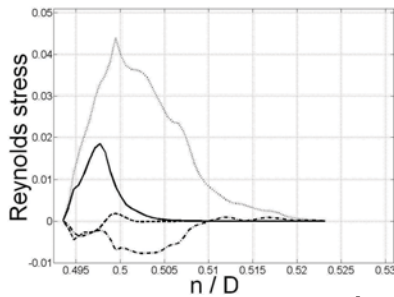
Sixth International Symposium on Turbulence and Shear Flow Phenomena
Seoul, Korea, 22-24 June 2009

Figure 14 – Reynolds stress, $Re = 1.1 \times 10^5$: —— ww, location 1; – – – uw, location 1; ···· ww, location 2; –·– uw, location 2
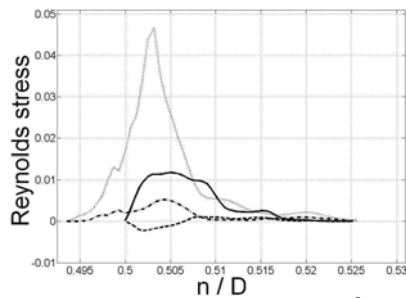

Figure 15 – Reynolds stress, $Re = 1.1 \times 10^5$: —— ww, location 3; – – – uw, location 3; ···· ww, location 4; –·– uw, location 4
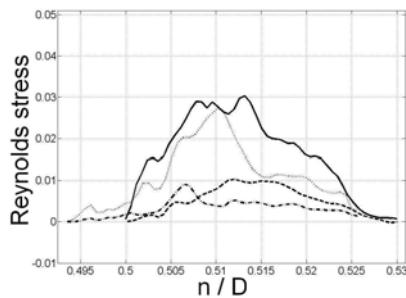

Figure 16 – Reynolds stress, $Re = 1.1 \times 10^5$: —— ww, location 5; – – – uw, location 5; ···· ww, location 6; –·– uw, location 6

Evolution of the Reynolds stresses for the high Reynolds number flow also help illuminate the local momentum transfer within individual dimples. Momentum transport by the fluctuations is higher at location 2 (Figure 14) versus location 1, as the value of the *ww* and *uw* components is approximately doubled. Reynolds stresses at location 3 (Figure 15) are the smallest for the supercritical case where the flow is reattached (c.f. Figure 5c). Location 4 (Figure 15) shows elevated values of *ww* and *uw* as the flow evolves from attachment to local detachment over this dimple. Reynolds stresses at locations 5 and 6 (Figure 16) have similar trends, although the trend occurs further into the flow (away from the surface of the golf ball) at location 6, indicating the onset of complete flow detachment.

SUMMARY

Direct numerical simulation (DNS) has been used to investigate the flow over a golf ball in the subcritical ($Re = 2.5 \times 10^4$) and supercritical ($Re = 1.1 \times 10^5$) regimes. An immersed boundary approach is applied to calculate the solution on grids ranging from 337×10^6 points for the subcritical flow to 1.2×10^9 points for the supercritical case. Flow visualizations of the instantaneous solution reveal the development of small-scale shear layers over dimples, consistent with the proposal of Choi, Jeon, and Choi (2006). Time-averaged traces of the velocity provide insight into the physical processes which characterize the flow, showing a recirculation within successive dimples for the supercritical case. Contours of the pressure coefficient on the surface provide some quantitative understanding of the behavior of the pressure near the golf ball, as well as the turbulent motion in the near-wake region. The pressure coefficient is -0.6 near 84 degrees for both physical regimes and seems to correspond with flow detachment occurring in this region.

Averaged values of the drag force are in the range of previous measurements. Wall-normal profiles of the mean velocity provide insight into the evolution of the flow near the wall, confirming complete flow detachment around 90 degrees for the subcritical regime; while local detachment and reattachment lead to complete flow detachment around 110 degrees for the high Reynolds number flow. Radial velocity spectra indicate secondary peaks at higher frequencies that appear to correspond to the small-scale structures developing over the dimple near separation. Reynolds stresses quantify the momentum contribution of the fluctuations near the body.

REFERENCES

Achenbach, E., 1972, "Experiments on the flow past spheres at very high Reynolds numbers", *Journal of Fluid Mechanics*, Vol. 54, pp. 565-575.

Balaras, E. and Yang, J., 2005, "Nonboundary Conforming Methods for Large-Eddy Simulations of Biological Flows", *Journal of Fluids Engineering*, Vol. 127, pp. 851-857, ASME.

Bearman, P. and Harvey, J., 1976, "Golf Ball Aerodynamics", *Aeronautical Quarterly*, Vol. 27, pp. 112-122.

Choi, J., Jeon, W., and Choi, H., 2006, "Mechanism of drag reduction by dimples on a sphere", *Physics of Fluids*, Vol. 18, pp. 0421702.1-4.

Davies, J., 1949, "The Aerodynamics of Golf Balls", *Journal of Applied* Physics, Vol. 20, pp. 821-828.

Maxworthy T., 1969, "Experiments on the flow around a sphere at high Reynolds numbers", *Journal of Applied Mechanics*, ASME, Vol. 36, p. 598.

Smits, A. and Ogg, S., 2003, "Aerodynamics of the Golf Ball", *Biomedical Engineering Principles,* Chapter 9, Kluwer Academic Press.

Smits, A. and Smith, D.R., 1994, "A new aerodynamic model of a golf ball in flight", *Science and Golf II: Proceedings of the World Scientific Congress of Golf II*, Chap.52, pp.340-347.

Yang, J. and Balaras, E., 2006, "An embedded boundary formulation for large-eddy simulation of turbulent flows interacting with moving boundaries", *Journal of Computational Physics,* Vol. 215, pp. 12-40.